Impact of Fuel Type on Toxic Emissions from a Non-premixed Boundary Layer Laminar Flame in Microgravity – A Numerical Study

Hui-Ying Wang

Impact of Fuel Type on Toxic Emissions from a Non-premixed Boundary Layer Laminar Flame in Microgravity - A Numerical Study

Hui Ying WANG

Corresponding author: Hui Ying WANG
Email: wang@ensma.fr
Telephone: 33 5 49 49 82 95

Institut Pprime (C.N.R.S.-U.P.R. 3346)
Département Fluide-Thermique-Combustion
ENSMA - BP 40109
Téléport 2, 1 av Clément ADER
86961 Futuroscope Chasseneuil Cedex
FRANCE

Abstract

Examples from non-premixed boundary combustion representative of fire in microgravity environment are presented. A low forced flow of 0.25 m/s is present, which is typical of air circulation speeds in a spacecraft. The numerical simulations have been conducted to evaluate the modes of heat transfer with an emphasis on a discussion about the effects of various fuels on chemical emissions such as soot, CO, CO_2 and unburnt hydrocarbons in reduced-gravity conditions. Typically, evaporation temperature is smaller for heptane than dodecane, and thus a lengthening of the heptane flame seems more pronounced as compared to that of dodecane flame with an increase in the visible flame zone by a factor of 2.3 times. A rapid regression rate of heptane due to the enhanced heat feedback contributes to an additional energy by a factor of 80% in heat release rate as compared to dodecane. In all the cases, only about 15% of the heat generated by an exothermic chemical reaction is supplied to the pyrolysis surface, and a large portion of energy is convected with the forward gas flow. The CO molar fraction reaches to a maximum of about 11% for dodecane and 8% for other fuels as ethylene, propane, propylene and heptane. The maximum mean value of CO concentration depends mainly on fuel injection rate, and appears practically insensitive to oxidizer flow velocity. Dodecane and heptane with a longer carbon chain produces more CO and less unburnt hydrocarbons than ethylene, propane and propylene. The existence of large unburnt toxic gas fuels even for a smaller flame size because of the absence of natural convection has important considerations for spacecraft fire safety due to smoke/gas incapacitation.

Key words: flame spread, radiation, convection, soot, toxic species, shear boundary layer, microgravity

Nomenclature listing

A_f	pre-exponential factor
A_s	effective soot surface area ($m^2.g^{-1}$)
C_γ	empirical parameter in soot model
d_f	flame stand-off distance (m)
d_p	diameter of the soot particulate (m)
D	diffusivity ($m^2.s^{-1}$)

f	mixture fraction
f_v	soot volume fraction
h	sensible enthalpy ($kJ.kg^{-1}$)
k	thermal conductivity ($W.m^{-1}.K^{-1}$)
K_{th}	thermophoretic velocity coefficient
L	convective length scale (m)
L_f	horizontal flame length (m)
L_v	pyrolysis heat ($kJ.kg^{-1}$)
$\dot{m}_s''$	mass loss rate of liquid fuel per unit surface ($kg.m^{-2}s^{-1}$)
N	soot number density per unit mass of mixture ($part.kg^{-1}$)
Nu	Nusselt number
p	pressure (Pa)
$\dot{q}_{conv}''$	convection heat flux ($kW.m^{-2}$)
$\dot{q}_{rad}''$	radiation heat flux ($kW.m^{-2}$)
$\dot{q}'''$	heat release rate per unit volume ($kW.m^{-3}$)
$\dot{q}_r$	radiative heat flux ($kW.m^{-2}$)
R	gas universal constant
Re	Reynolds number
r_s	direction vector of the radiation intensity
s	stoichiometric coefficient
Sc	Schmidt number
T	gas temperature (°C)
T_b	boiling temperature of liquid (K)
T_g	gas temperature (K) at the center of the adjacent gas phase cell
T_s	surface temperature of liquid (K)
T_γ	empirical parameter in soot model
t	time (s)
u	velocity ($m.s^{-1}$)
u_n	normal component of velocity at the surface
u^{th}	thermophoretic velocity ($m.s^{-1}$)
V_{ox}	oxidizer flow velocity ($m.s^{-1}$)
X_F	fuel mole fraction
Y_F	fuel mass fraction
$Y_{F,g}$	fuel mass fraction at the center of the adjacent gas phase cell
$Y_{F,s}$	fuel mass fraction at liquid surface
Y_O	oxygen mass fraction
Y_P	product mass fraction
Y_s	soot mass fraction
x, y, z	coordinates system in numerical simulation
W_F	molar weight of liquid fuel ($kg.kmol^{-1}$)
W_m	molar weight of mixture ($kg.kmol^{-1}$)

Greek

ρ	volume density ($kg.m^{-3}$)
ρ_s	soot volume density or volume density at the surface ($kg.m^{-3}$)
ε_s	surface emissivity
σ	radiation constant

Ω	solid angle
τ_{mix}	key mixing timescale (s)
τ_{ij}	viscous stress
μ	laminar viscosity ($kg.m^{-1}.s^{-1}$)
δn	distance between the surface and the center of the adjacent gas phase cell
$\dot{\omega}_{s,N}^{'''}$	soot inception rate ($kg.m^{-3}.s^{-1}$)
$\dot{\omega}_{s,G}^{'''}$	heterogeneous surface growth rate ($kg.m^{-3}.s^{-1}$)
$\dot{\omega}_{s,O}^{'''}$	soot oxidation rate ($kg.m^{-3}.s^{-1}$)
ΔH_c	heat of combustion ($kJ.kg^{-1}$)

Introduction

In the context of active space exploration, the most likely scenario of a fire accidentally initiated and spreading on board of spacecraft has been widely studied for several decades [1-6]. Air entrained from a predominant natural convection at Earth gravity generates a self-sustaining flame which is almost unaffected by presence of a low forced flow of 0.1–0.3 m/s, which is typical of air circulation speeds in a spacecraft. In normal gravity, radiation in fires was considered as the primary cause of fire growth only when the flame size became greater than about 40 cm, at which point these large flames yielded substantial soot and luminous radiation [7]. In typical concurrent-flow, the pyrolysis rates are dominated by convection, and the external flow velocity influences both the flame length and the heat flux from the flame to the solid surface. In addition, gas phase chemical kinetics may affect the spread rate and even cause extinction (blow-off) of the flame at high flow speed. At microgravity, the superior mode of flame spread over a surface of combustible material translates to a co-current boundary layer type even at very-low-flow speeds [1]. Experiments [8] indicate that radiation is predominant mode of heat transfer because of the absence of natural convection at microgravity with large and consistent radiative loss fractions in a range of 0.45 to 0.6 compared to 0.07 and 0.09 at Earth gravity, for various fuels, pressures, oxygen mole fractions, and flow rates. Quantitative measurements [9] show peak soot-volume fractions about twice as high at microgravity than Earth gravity for 50% C_2H_2 and 50% N_2-air flames.

An optical setup and its associated post-processing have been designed [10] in an effort to map soot volume fraction, soot temperature and soot-related radiative loss in an axisymmetric flame spreading over solid samples in microgravity environment. The study [11] assesses the consistency of the two optical techniques (BMAE and B2CP), used in the previous work [10], contrasting an experimental frame in a flame spreading over an electrical wire in microgravity. Using a signal modeling that processes fields delivered by a numerical simulation [12] of the configuration as inputs, the fields of local radiative balance within the flame are computed, and significant discrepancies were disclosed locally between the fields originating from the synthetic BMAE and B2CP inputs. Some meaningful illustrations of fire hazards at microgravity assess flame spread over electric wire [13] or small solid samples [14] via the study of flammability and combustion of solid materials. Concomitant flames spreading over the coating of parallel cylindrical wires in an air flow parallel to the wires in microgravity has been studied [15] for dealing with the issue of the potential interaction

among spreading flames. Through the elimination of buoyancy, only at oxygen fraction of 30%, flame temperature is high enough that flame spread over solid fuel beds is achieved [16]. The consensus provided by these works [7, 14, 16, 17] is that flame spread is highly configuration dependent, varying with factors including sample size (length, width, thickness), confinement size (container or tunnel dimensions), and gas-phase flow time, diffusion time, chemical time and the solid heat-up/ conduction times. The influences of some of these parameters on chemical species are profoundly affected by gravity-induced buoyant flows. Flame spread over liquid fuels encompasses practically all solid-fuel flame spread phenomena, plus liquid-phase flow effects. Typically, evaporation temperature is smaller for liquid than solid fuels, thus flame spread rate is higher [17]. Flame spread calculations have employed optically thin radiation models with constant absorption coefficient [18, 19]. Numerical simulations have been performed [2] to determine the effects of a dimensionless volume coefficient on flame quenching and its stand-off in a shear reactive boundary layer in the absence of natural convection. Several microgravity researches [3, 4] have shown that a blue unstable flame, negligible radiative feedback, may change to a yellow shorter flame, significant radiative feedback with an increase of a dimensionless volume coefficient which favours soot formation. Compared with Earth gravity flames, microgravity flames have much greater tendencies to emit soot due to long residence times for soot formation and plus broader regions in which composition and temperature are favorable for soot formation [4, 17]. Co-current flame spread over a solid plate could then be linked to a critical soot concentration [20] controlling the trailing edge quenching. An important finding [21] associates with the competing effects of diffusion, fuel injection and oxidizer flow velocity in microgravity on the role of soot production and consumption in flame quenching.

There is self-similar solution [22, 23] to the problem of blowing in a reacting boundary layer without the consideration of radiative heat exchange. In order to overcome gravity effects, the flow velocity would have to be so large that the radiant flux from the flame approximately balances surface re-radiation, and that there is not an external heat flux, and then the forced-flow flame spread is primarily determined by convective heat flux. Only in this case, it can be concluded [22] that an increase of mass transfer parameter brings to decrease of temperature gradient, and as a result, a decrease of heat flux. At very-low-flow speeds in microgravity, flame spread depends on the radiation flux downstream the leading edge, an important distinction compared to the case at high flow speed which normally depends only the forced flow velocity. As a consequence, the absence of radiation heat transfer in the self-similar solution [22, 23] prevents complete validation for flame spread at very-low-flow speeds, because in microgravity, an increase of mass transfer parameter brings to increase of heat flux via radiation with an ever-thickening flame.

Despite the progress that is apparent in the existing literature, most previous studies at microgravity are limited to soot-related flame spread with a selected gas [1-6] or solid combustible materials [7, 10, 12, 14]. Motivated by these observations, this theoretical research looks specifically the consequences of various types of fuel on toxic emissions as soot, carbon monoxide and unburnt hydrocarbons. Gas fuels as ethylene, propane and propylene could originate e.g. from decomposition of most solid combustible materials [14] in spacecraft when they are exposed to fire. Liquids (mineral oil, synthetics, etc.) could originate e.g. from leaking transformers, generators or other machinery. Flame spread over liquid fuels as heptane and dodecane has been widely studied [17] although these fuels are never used in

spacecraft. The detailed diagnostics including toxic species measurement by using a gas analyzer creates an insurmountable difficulty under microgravity conditions even using a scaled-down facility due to the limited space and duration of about 20 s during parabolic flights [3, 4, 21]. A complement numerical study on which the decision making process regarding fire safety in manned spacecraft depends increasingly, appears necessary. An acetylene/benzenz based-soot model [24] is used for soot calculation over an insulated electrical wire in microgravity under the assumption of pure ethylene from the decomposition of low density polyethylene [12]. The same soot model [24] was also applied to an ethylene diffusion flame over a flat plate at microgravity [5]. A detailed ethylene kinetic reaction mechanism is required for providing the local concentration of soot precursory species, such as acetylene (C_2H_2), benzene (C_6H_6), phenyl (C_6H_5) and OH. When the measured soot volume fraction in ethylene diffusion flame at microgravity was compared to the calculations [5, 12], the models validity was confirmed only at some locations. It is worthwhile to note that the semi-empirical parameters in the acetylene/benzenz based-soot model [24] are limited to a selected fuel as ethylene for involving the inception, coagulation, surface growth and oxidation processes. Due to this limitation, a modeling effort is initiated to look for soot calculation for other fuels by implementing LSP (Laminar Smoke Point) concept [25] in FDS6.7 [26]. The advantage of the present soot model is that the LSP height of any practical fuels can be measured, although the exact elementary reactions are generally unknown. This provides a general and practical solution for soot modeling in multi-fueled fires. Although the basic mechanisms of the flame chemical kinetics are the same with or without gravity, the relative magnitudes and characteristics of the transport of thermal energy and reactants are different. For a free-burning fire, the buoyant flow at Earth gravity with a velocity of several meters per second enhances the mass flow rate of oxygen at the flame location, allowing a low toxic emission [27]. Compared with Earth gravity flames, microgravity flames have much greater tendencies to emit large toxic emissions, which result in the majority (80%) of fire fatalities due to smoke/gas incapacitation, even for a smaller flame size because of the absence of natural convection.

2. NUMERICAL MODELLING

In order to configure high-fidelity geometric simulations [3, 4], the starting point of the analysis is the set of three-dimensional elliptic, reacting flow equations that governs the phenomena of interest here. The unsteady equations are discretized and iteratively solved. A detailed description of the physics-based equations and the numerical method are presented in FDS6.7 user guide [26] and references therein. In the current work, only the essential physical processes on hydrodynamic, combustion and soot models are provided.

2.1 Hydrodynamic model

The hydrodynamic model consists of the transient equations of mass, momentum, energy and species conservation.

Mass conservation:

$$\frac{\partial \rho}{\partial t} + \nabla \cdot (\rho u) = 0 \qquad (1)$$

Momentum conservation:

$$\frac{\partial \rho u}{\partial t} + \nabla \cdot (\rho u u) = -\nabla p - \nabla . \tau \tag{2}$$

Energy conservation:

$$\frac{\partial \rho h}{\partial t} + \nabla \cdot (\rho h u) = \nabla \cdot (k \nabla T) + \dot{q}''' - \nabla \cdot q_r \tag{3}$$

Chemical species conservation:

$$\frac{\partial \rho Y_i}{\partial t} + \nabla \cdot (\rho Y_i u) = \nabla \cdot (\rho D \nabla Y_i) + \dot{\omega}_i''' \tag{4}$$

In the Shvab-Zeldovich energy equation (Eq.3), h represents the sensible enthalpy. Since unit Lewis number is used, the enthalpy flux from the diffusing species is taken into account through the heat release rate by employing both Fick's Law and species conservation [25]. The thermophoretic velocity of soot particulate due to temperature gradients, u^{th}, can be added in the convective transport term in Eq.4.

$$u^{th} = \frac{K_{th} \mu}{\rho T_g} \cdot \mathrm{grad}(T) \tag{5}$$

2.2 Combustion model

Reactions from Westbrook [28] are assumed to account for carbon monoxide production via the two sequential, semi-global steps.

$$C_m H_n + \left(\frac{m}{2} + \frac{n}{4}\right) O_2 \rightarrow m\,CO + \frac{n}{2} H_2O \tag{6}$$

$$CO + \frac{1}{2} O_2 \Leftrightarrow CO_2 \tag{7}$$

The primitive fuel oxidation is a fast chemistry, and its reaction rate in Eq.4 is calculated as,

$$\dot{\omega}_i''' = \frac{d \rho Y_F}{dt} = -\frac{\rho}{\tau_{mix}} \min(Y_F, \frac{Y_O}{s}) \tag{8}$$

The key mixing timescale in Eq.(8), τ_{mix}, is supposed to relate approximately to the processes of diffusion and chemical reaction times [26]. To create a mixed reaction mechanism, fast chemistry is combined with finite-rate reversible carbon monoxide reaction (7) by using the modified Arrhenius parameters from Andersen [29].

2.3 Soot formation model

The processes of soot inception, heterogeneous surface growth and oxidation are applied to the balance (cf. Eq.4) between transport and soot production via the respective source terms :

$$\dot{\omega}_i''' = \dot{\omega}_{s,N}''' + \dot{\omega}_{s,G}''' + \dot{\omega}_{s,O}''' \tag{9}$$

The soot inception process can be described in terms of Laminar Smoke-Point (LSP) concept [25].

$$\dot{\omega}_{s,N}''' = A_f \rho^2 T^{2.25} \frac{f - f_{st}}{1 - f_{st}} \exp(-2000/T) \qquad (10)$$

where the pre-exponential factor, A_f, accounts for the sooting propensity of a specific fuel. The conserved Schvab-Zeldovich, mixture fraction, f, is the key scalar variable in the soot inception process.

$$f = Y_F + \frac{1 + Y_P}{s} \qquad (11)$$

The sooting propensities of various fuels are accounted for via a pre-exponential factor A_f, which is in reversely proportional to its LSP height, L_{Fuel}.

$$\frac{A_{f,Fuel}}{A_{f,C_2H_4}} = \frac{L_{C_2H_4}}{L_{Fuel}} \qquad (12)$$

A summary of $A_{f,}$ calculated according to Eq.(12) for the used hydrocarbon fuels in the current work, is pre-tabulated in Table 1.

Table 1. Summary of the pre-exponential factor, $A_{f,}$ for various fuels

Fuel type	ethylene	propane	propylene	heptane	dodecane
factor A_f	4.1×10^{-5}	2.6×10^{-5}	14.6×10^{-5}	2.9×10^{-5}	3.1×10^{-5}

The surface growth rate [30] is derived from the local temperature, T, soot number density, N, and mole fraction of the parent hydrocarbon, X_F.

$$\dot{\omega}_{s,G}''' = C_\gamma \rho T^{1/2} X_F \exp(-T_\gamma/T)\ N^{1/3} (\rho Y_s)^{2/3} \qquad (13)$$

The empirical parameters, C_γ and T_γ, in the heterogeneous processes of surface growth, are calibrated by comparison to detailed measurements of soot production in a non-premixed flame [30]. Rather less information is generally available on soot number density, N, than the soot surface area per unit mass of soot, measured approximately with a value of $A_s=160\times10^3$ m^2/kg, but it is a combination which provides a mean primary particle diameter, d_p.

$$d_p = \frac{6}{\rho_s A_s} \qquad (14)$$

Diameter of the primary soot particulates, derived from Eq.(14), is with a value of roughly $d_p = 0.02\ \mu m$. By assuming a spherical shape of soot particulates, the soot number density per unit mass of mixture, N, is evaluated from soot mass fraction, Y_s,

$$N = \frac{6 Y_s}{\pi d_p^3 \rho_s} \qquad (15)$$

The temperature dependence of soot oxidation in a laminar diffusion flame is modelled [26, 31], and its specific rate is expressed as a function of soot and oxygen concentrations (mol/cm^3) by,

$$\dot{\omega}_{s,O}''' = -4.7\times10^{10} [Ys][Yo] \exp(-211000/RT)$$

(16)

2.4 Heat balance at interface

The liquid layer is assumed to be thermally-thick, a one-dimensional heat conduction equation for the condensed phase temperature $T_s(x, t)$ is applied in the direction x pointing into the liquid phase [26]. The boundary condition on the front surface of a liquid is established via a heat balance:

$$-k_s \frac{\partial T_s}{\partial x}(0,t) = \dot{q}''_{conv} + \dot{q}''_{rad} - \dot{m}''_s L_v \tag{17}$$

where the point x=0 represents the surface of liquid. For a laminar flow, the convective heat flux, $\dot{q}''_{conv}$, at the surface is directly determined via Fourier law [26], and written :

$$\dot{q}''_{conv} = k \frac{T_g - T_s(0,t)}{\delta n} \tag{18}$$

where δn is the distance between the surface and the center of the adjacent gas phase cell.

The radiant heat flux, $\dot{q}''_{rad}$, at the liquid surface is calculated from the radiant intensity for situations where the wall is a diffusively reflecting and emitting surface [26].

$$I(r_s, \Omega) = \frac{\varepsilon_s \sigma T_s^4}{\pi} + \frac{1-\varepsilon_s}{\pi} \int_{n.\Omega} |n.\Omega'| I(r_s, \Omega') d\Omega' \tag{19}$$

The radiant intensity is found by solving the radiation transfer equation (RTE) with a ray-based method, known as the discrete ordinate method [26]. At microgravity, soot emission is far away from the flame leading edge where only the contribution from gas-phase radiation from H_2O and CO_2 is significant. Thus, a wide band model is used by taking into account the spectral dependence of absorption coefficient in RTE [26].

The local liquid burning rate at the flame base is determined from the overall conservations of mass and energy at interface [32].

$$\dot{m}''_F = \frac{\rho D}{L} Nu \ln\left[\frac{1-Y_{F,\infty}}{1-Y_{F,i}}\right] \tag{20}$$

The mass fraction of liquid fuel in gas phase, $Y_{F,g}= Y_{F,i}$, depends on its surface temperature, $T_s(0, t)$, as :

$$Y_{F,i} = \frac{W_F}{W_m} \exp\left[-\frac{L_v W_F}{R}\left(\frac{1}{T_s} - \frac{1}{T_b}\right)\right] \tag{21}$$

The mass balance at the burning boundary is established as :

$$\dot{m}''_F = u_n \rho_s Y_{F,s} - (\rho D)_s \frac{Y_{F,g} - Y_{F,i}}{\delta n} \tag{22}$$

where u_n is the normal component of velocity at the surface pointing into the flow domain. For the laminar boundary layer flow at very low speeds in microgravity, the tangential velocity over the liquid surface tends to zero.

For a laminar flame, material diffusivity, D, thermal conductivity, k, and viscosity, μ, are approximated from kinetic theory [26] because its temperature dependence is important in combustion scenarios. Liquid fuels as heptane and dodecane are used in the current work, and the detailed informations about its thermo-physical and combustion properties [32] are provided in Table 2.

Table 2. Thermo-physical and combustion properties of heptane and dodecane

Property	Heptane	Dodecane
Conductivity k (W/m.K)	0.17	0.14
Density ρ (kg/m^3)	684	750
Heat capacity C_p (kJ/kg.K)	2.24	2.21
Pyrolysis heat, L_v (kJ/kg)	321	256
Heat of combustion, ΔH_c (kJ/kg)	44500	44147
Boiling temperature T_b (°C)	98	216

2.5 Computational domain and boundary conditions

The numerical set up is displayed in Fig.1(a,b), which has been chosen in order to stick as much as possible to the experimental configuration [3, 4]. Due to the limited space and amount of feed gases available in parabolic flight facilities, only a small square gas burner with dimensions of L_p=W_p=5 cm is placed in the center of a large enclosed combustion chamber. Porous burner has been used regularly in an attempt to simplify experiments by avoiding the coupling between heat feedback from the flame and fuel supply so that longer experimentation time can be achieved. Because the pyrolyzed fuel and oxidizer are initially separated, the flame is primarily of the diffusion type. The characteristics of such a boundary layer diffusion flame (cf. Fig.1a) are dictated by mixing considerations between the fuel velocity ($V_F \cos\theta$) and the oxidizer flow velocity ($V_{ox} \cos\theta$).

In the previous studies [2, 5, 6] on such a diffusion flame (cf. Fig.1a), it was found that *a priori* estimates of the computational domain of $8L_p$ in the windward direction (x), and $4L_p$ in both the lateral (y) and normal (z) directions seems to be enough to apply zero gradient conditions on the free boundaries such as at two sides, top and outlet of the domain for the farfield boundary values of the variables. An excessive domain extension needs the use of a highly compressed grid system, and build-up of numerical error could produce spurious results over the course of a calculation [26]. The gas burner is embedded in a stainless-steel plate at z=0 with a short entrance length of 5 cm. As the experiment, the oxidizer flow is with an elevated oxygen concentration environments of 35%, and a constant velocity, V_{ox}, of 0.25 m/s was prescribed at the inlet of x/L_p=-1. The flame boundary condition was prescribed by the experimental fuel supply rate varying from 3 to 5 (g/m^{2}s) over the gas burner surface. Over the burning surface of condensed fuel as heptane and dodecane, the pyrolysis rate is derived from a heat balance at interface (cf. Eq.20).

A proper cell sensitivity analysis by varying the grid spacing from 2 to 1 mm was performed on the predicted quantities in the previous study [5]. A deviation of roughly 5% is observed

for the flame temperature solely near the leading edge by varying the grid spacing from 2 to 1 mm. The computational domain consists of multiple meshes which can be treated with 20 processors through parallel processing of a Linux cluster. With a mesh size of 2 mm, a typical simulation during a physical time of 10 s requires roughly 150 CPU hours. A reduction in the grid size to 1 mm results in a significant reduction in the time step ($\Delta t < 10^{-5}$ s) due to the CFL (Courant-Friedrichs-Lewy) stability constraint. With each halving of the grid size, the time required for the simulation increases by a factor of $2^4=16$ (a factor of two for each spatial coordinate, plus time), making practical flame simulations difficult. The grid system containing 200 x 100 x 75 cells with a mesh size of 2 mm is extensively used for a low Reynolds number flow [2, 5, 6], since it is considered as the best trade-off between accuracy and cost for a three-dimensional reacting flow simulation.

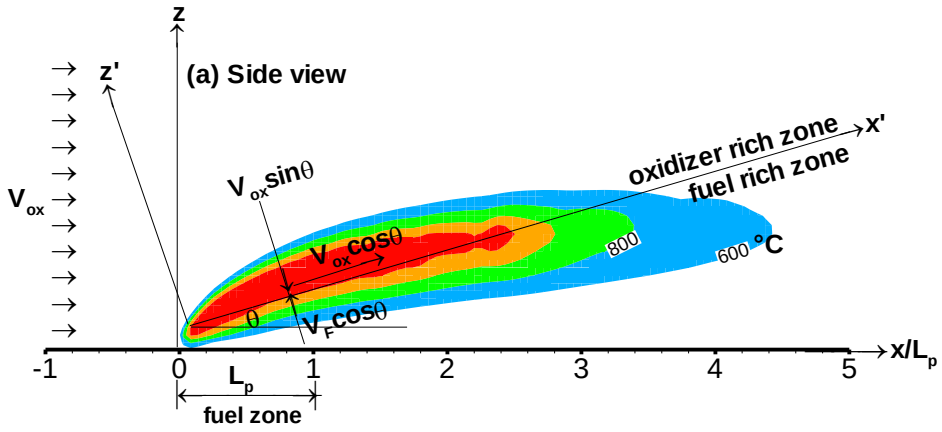

1a) boundary layer flame (side view)

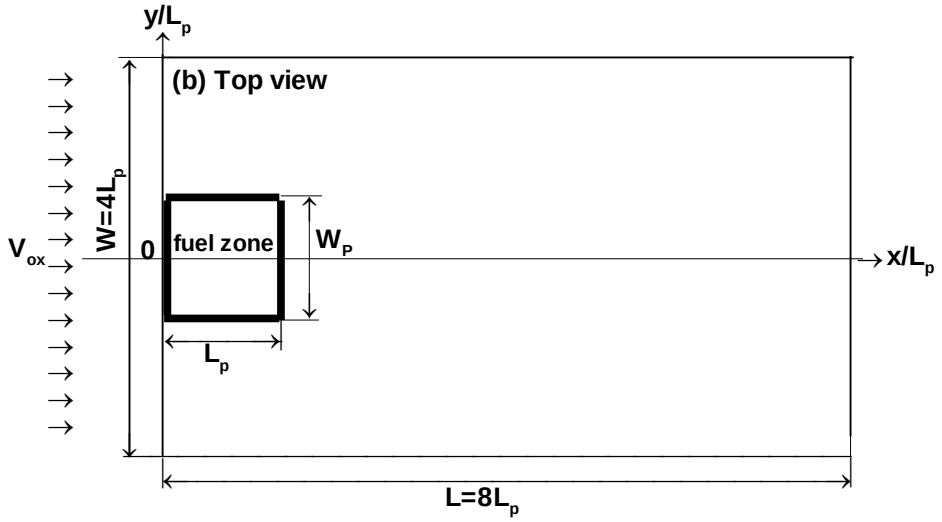

1b) disposition of the fuel zone (top view)

Figure 1. Computational domain and the coordinate system

3. Results and discussions

The modelling was carried out for a series of 8 different scenarios (Cases 1-8) with variations in fuel type, burning rate and oxidizer flow velocity, as provided in Table 3. By means of parabolic flights, porous burner has been used [3, 4] in an attempt to simplify experiments by injecting ethylene with a constant burning rate of 5 g/m^{2}s so that longer experimentation time can be achieved. The gas fuels as propane and propylene with a constant burning rate of 5 g/m^{2}s and the condensed fuels as heptane and dodecane are numerically simulated.

Table 3. Simulations conducted fire scenarios

Fire scenarios	Fuel type	Burning rate (g/m^{2}s)	Oxidizer flow velocity, V_{ox} (m/s)
Case 1	ethylene	5 (constant)	0.25
Case 2	ethylene	4 (constant)	0.25
Case 3	ethylene	3 (constant)	0.25
Case 4	ethylene	5 (constant)	0.125
Case 5	propane	5 (constant)	0.25
Case 6	propylene	5 (constant)	0.25
Case 7	heptane	variation with time (Fig.3)	0.25
Case 8	dodecane	variation with time (Fig.3)	0.25

The predicted liquid temperature and mass flow rate for evaporated fuel as heptane and dodecane being the function of longitudinal co-ordinate x on the central plane (y=0, cf. Fig.1) at the different times are provided in Fig.2(a, b) and 3(a, b). A flame spreads over a liquid fuel by first preheating the virgin fuel to its vaporization temperature of about 60°C and 160°C respectively for heptane and dodecane, pyrolyzing it, and igniting the flammable mixture of pyrolyzate and oxygen. The hot reacting gases and post-combustion gases generated in the pyrolysis region move ahead of the pyrolysis front in the form of a flame transferring heat to the virgin fuel downstream. The flame would effectively move into an ever-thickening boundary layer (cf. Fig.1) making an unsteady solution intractable. The pyrolysis rate increases with the liquid temperature, and asymptotically reaches a limit once the liquid temperature reaches roughly a steady value. Once a steady state is established over liquid surface, the heat flux to the surface is used entirely for pyrolysis rather than a further temperature rise to supply a permanently burning flame. The pyrolysis rate exhibits a peak of about 30 and 20 g/m^{2}s respectively for heptane and dodecane near the leading edge, and a sharp decrease beyond that region. The burning rate of dodecane approaches zero for the liquid temperature below 130°C to reach a limiting length of x/L_p=0.5, sufficient heat input from the flame is needed at the pyrolysis front to increase surface temperature. The possibility of reaching a limiting length is expected to be greater for dodecane in lower-speed flow in microgravity due to its high boiling temperature (cf. Tab.2).

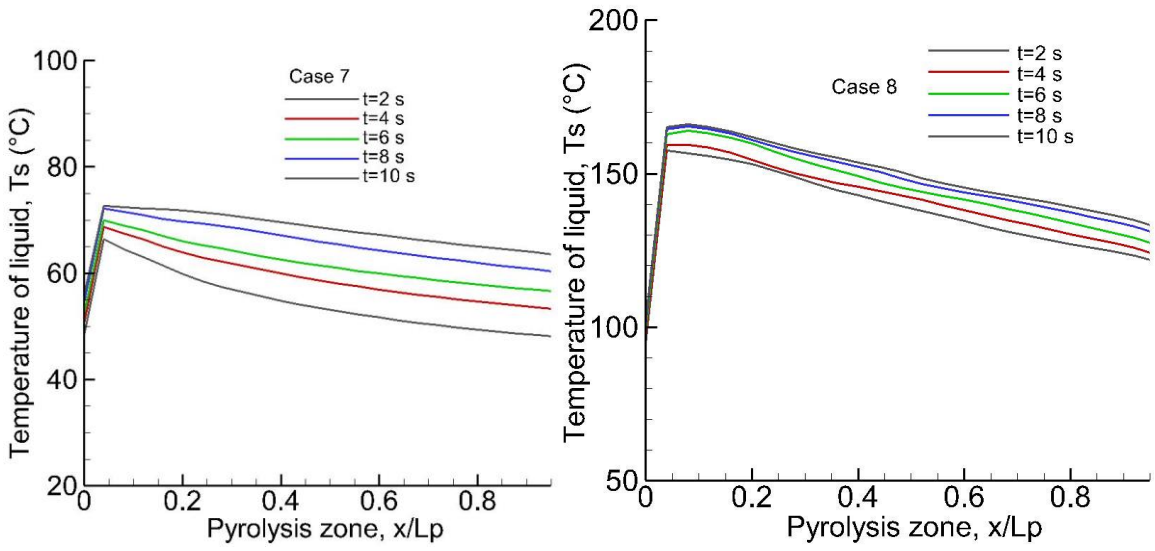

2a) Heptane 2b) Dodecane

Figure 2. Spatial distribution of the predicted surface temperature of heptane and dodecane at the different times

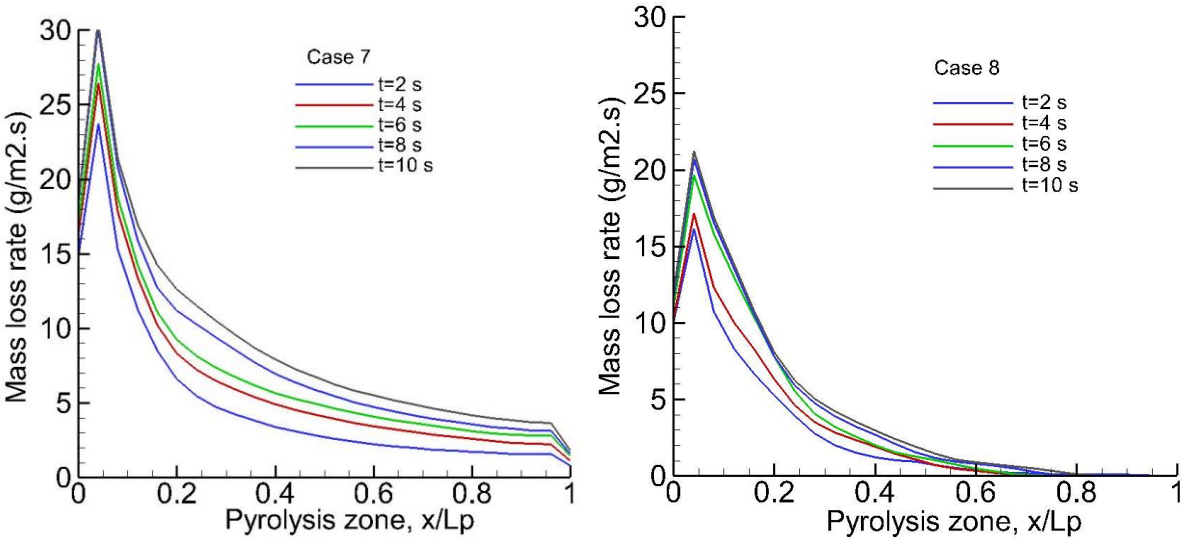

3a) Heptane 3b) Dodecane

Figure 3. Spatial distribution of the predicted pyrolysis rate over heptane and dodecane surfaces at the different times

Microgravity reduces buoyancy enough to enable a boundary layer diffusion flame even for a low oxidizer flow velocity of 0.25 m/s, as shown in Fig.4 for a series of iso-contours of temperature above 600°C. The fuel pyrolysis rate which is generated in the pyrolysis region controls flame length, and a concurrent flame spread reaches a steady rate with a limiting flame length. The pyrolysis rate of condensed fuel reaches to a maximum at the steady mode during about 10 s (cf. Fig.3), conducting to the most devastating fire scenario with the most important flame length and toxic emissions. The flame length, L_f, is defined as the distance of the 600°C contour from the leading edge, and its stand-off distance, d_f, from the flat plate, e.g., L_f=0.25 m and d_f=0.03 m for heptane (Case 1). This definition is chosen since the

majority of the radiation is derived from the visible part of the flame with a temperature higher than 600°C, where soot particles are radiating heat [33]. Near the leading edge, the energy released during combustion allows the gas temperature to raise above 1500°C (cf. Tab.3) for ethylene/propane/propylene, and 1400°C for heptane and dodecane. At microgravity, the reactive boundary layer is significantly lifted above the fuel surface once away from the leading edge with a very important augmentation of the stand-off distance, and in parallel a lengthening of the flame. A rapid regression rate of heptane (cf. Fig.3a) contributes to a larger flame zone with an increase by a factor of 25% in flame length as compared to the fuel with burning rate of 5 g/m^{2}s. Dodecane gives a shorter flame length due to its limiting pyrolysis length of x/L_p=0.5 (cf. Fig.3b). An increase in pyrolysis rate for heptane results in an increase in the flame length (cf. Fig.4) up to x/L_p=7. The fire development along heptane seems more pronounced as compared to dodecane with an increase in the visible flame zone by a factor of 2.3 times due to a significant difference in its boiling temperature (cf. Tab.2). Flame propagation from an existing fire is responsible to spontaneous ignition of an inflammable object exposed within the flame length for a certain period of time.

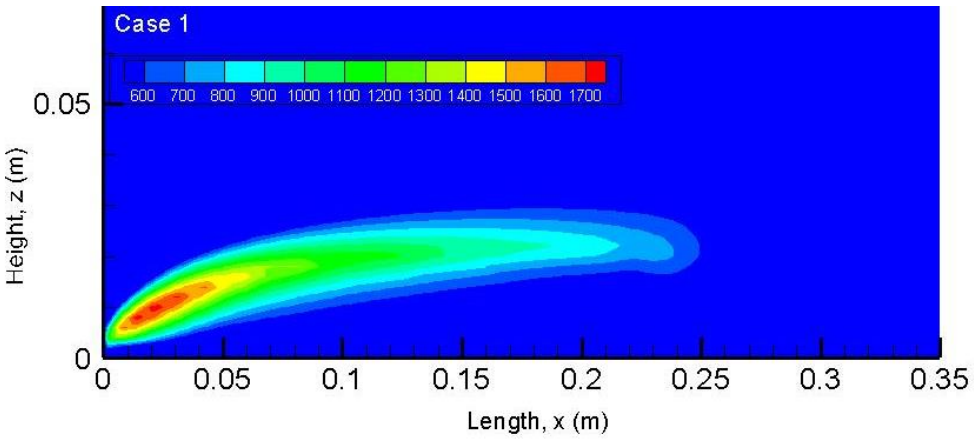

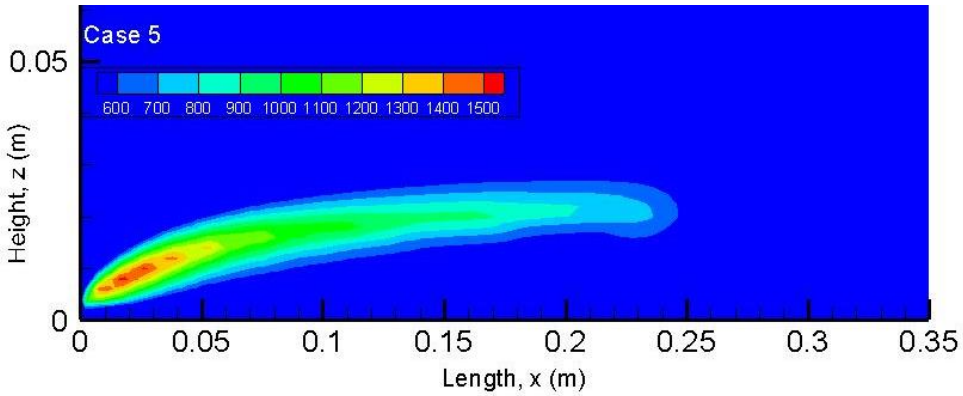

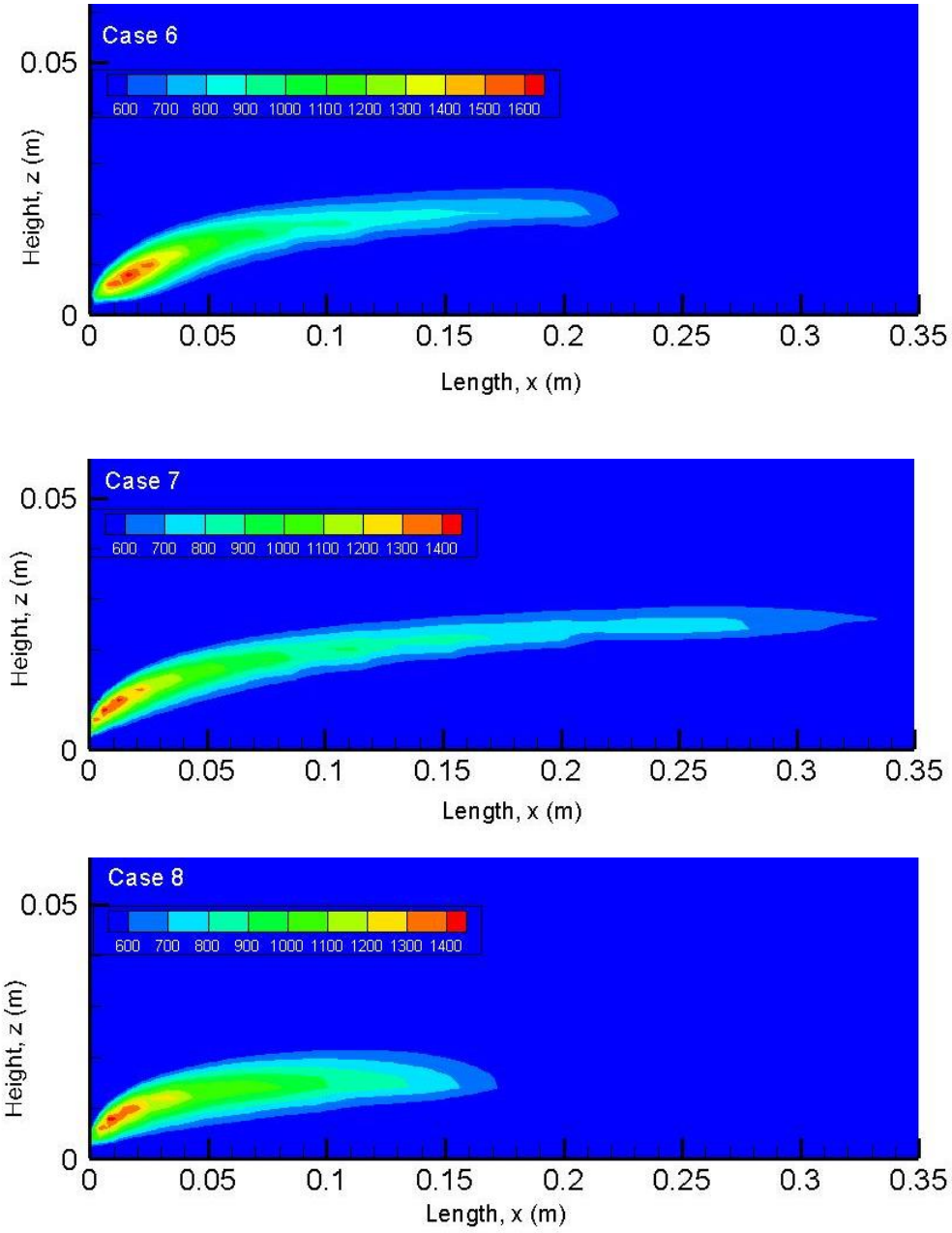

Figure 4. Geometric characteristics of a co-current flame at the steady mode (t=10 s) with the 600°C contour for ethylene (Case 1), propane (Case 5), propylene (Case 6), heptane (Case 7) and dodecane (Case 8)

As an illustration, iso-contours of gas temperature on the cross-stream plane for ethylene (Case 1) at the axial location of $x/L_p=2$ at microgravity are shown in Fig.5. The flames develop strongly three-dimensional features far away from the trailing edge. The extent of the flame in cross-stream plane surpasses significantly the pyrolysis zone $[-0.025\,\text{m}, 0.025\,\text{m}]$ due to the lateral mixing through the edge of the flame.

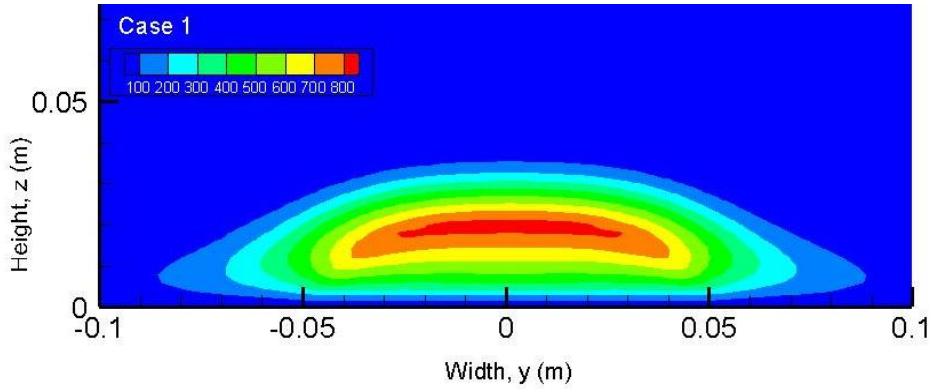

Figure 5. Iso-contours of gas temperature (°C) at the steady mode (t=10 s) on the cross-stream plane for ethylene (Case 1) at the axial location of $x/L_p=2$

As an illustration, the influences of fuel type as ethylene, heptane and dodecane on iso-contours of soot volume fractions on the axis of symmetry are depicted in Fig.6. The microgravity flames are sootier and the amount of soot is affected significantly by the fuel type, temperature and pyrolysis rate. Soot is located mainly below the flame zone (cf. Fig.4) with a similar trend for all type fuel. Fujita et al. [34] observed that soot particles trajectories inside a laminar boundary layer diffusion flame at microgravity do not follow exactly the gas movement due to thermophoretical effects. This is evidenced by a significant deviation of soot particles from the flame sheet due to a significant temperature gradient which prevents soot particles approaching the flame. The strongest soot production is placed over the pyrolysis zone where the fuel is rich for heptane and dodecane due to a decrease in soot oxidation, and over the plate surface downstream the fuel injection zone with a low burning rate (Case 1). Soot volume fraction of the heptane flame with a high burning rate (cf. Fig.3a) increases by a factor of about 4 times as compared to the heavily sooting ethylene flame (Case 1). With an increase of the pyrolysis rate from 20 for dodecane to 30 g/m^2s for heptane in peak (cf. Fig.3), the excessive fuel serves to increase the soot level from 18 to 45 ppm in peak. As compared to the other fuels, an additional burning rate of almost 5 times (cf. Fig.3) for heptane contributes to a significant soot stratification in the forward layer flow. Less soot formation results in an increase of gas temperature (cf. Fig.4, Cases 1, 5, 6), and inversely, more soot conducts to a decrease of gas temperature via radiation loss (cf. Fig.4, Cases 7-8).

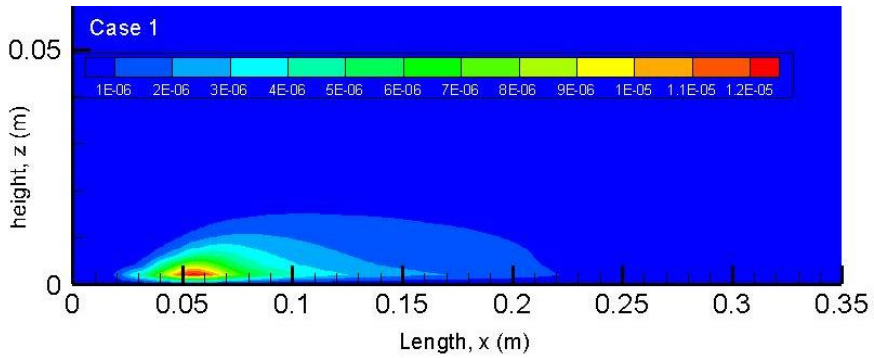

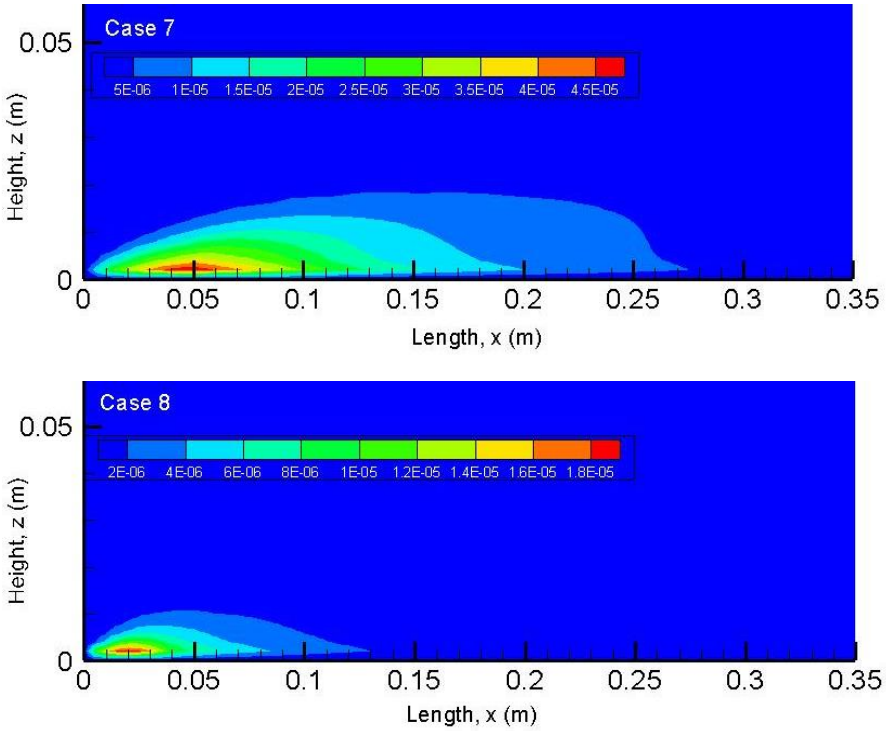

Figure 6. Iso-contours of soot volume fraction at the steady mode (t=10 s) for ethylene (Case 1), heptane (Case 7) and dodecane (Case 8)

As an illustration, iso-contours of soot on the cross-stream plane for ethylene (Case 1) at the axial location of $x/L_p=2$ are shown in Fig.7. The thickness of soot formation in width direction (y) becomes mostly significant with a three-dimensional behavior due to the convective and diffusive transports nearby the edge of the flame.

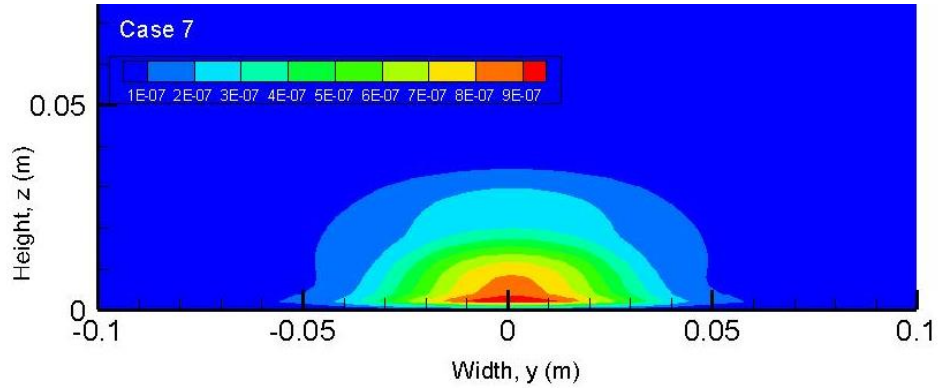

Figure 7. Iso-contours of soot volume fraction at the steady mode (t=10 s) in cross-stream for ethylene flame (Case 1) at the axial location of $x/L_p=2$

In microgravity conditions, the sooting behaviour of ethylene laminar diffusion flame is characterized by using the laser induced incandescence technique (LII) [3, 4]. The basic principle of LII relies on the detection of the thermal radiation from the soot particles that have been heated up to vaporization temperature by means of high energy laser pulse. The measured soot volume fraction distribution is converted from LII intensity image, and its accuracy depends on the accuracy of the proportionality constant required for correction due to attenuations of both the laser beam and the collected signal. Given in Fig.8 is the comparison between the predicted and the measured soot volume fractions for ethylene (Case

1) across the height, z, at various axial locations x/L_p=0.4, 0.8, 1.2, 1.6, 2 and 2.4 for V_{ox}=0.25 m/s and burning rate of 5 g/m^{2}s. The LSP model gives a relatively good agreement with the measurement in the general shape, and an over-prediction of about 20% is found at x/L_p>2 far away from the tailing edge. The disagreement between the prediction and the measurement might be caused by neglect of both the endothermicity of soot formation reactions and soot oxidation via OH radicals which becomes more pronounced downstream the tailing edge. In spite of the difference, the comparison between the numerical and the experimental results is deemed satisfactory, considering all the simplifying assumptions made in the global soot model and uncertainties in measuring local soot concentration during parabolic flights.

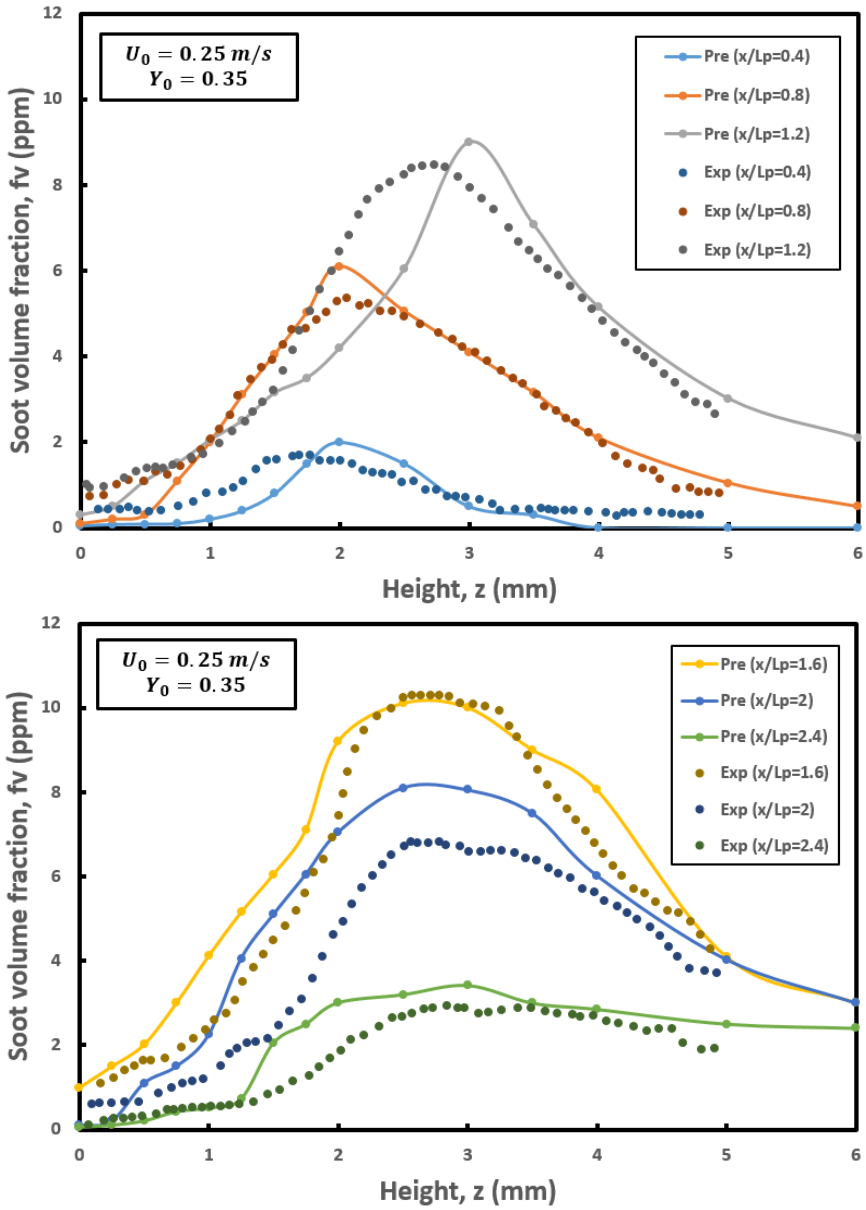

Figure 8. Comparison between computation and experiment for soot volume fraction at different axial locations, x/L_p , for ethylene flame (Case 1)

Soot formation is averaged through the integrated smoke layer in the z direction, as follows :

$$\overline{F}(x) = \int_{z=0}^{Z_{max}(x)} f(x,z)dz / Z_{max}(x) \qquad (23)$$

where f is soot volume fraction, and Z_{max} (x) the height so that f(x,z)=0 for $z>Z_{max}(x)$ at a given x. The mean value, $\overline{F}(x)$, of the toxic emissions as soot is examined in Fig.9a in the windward direction for the ethylene flame as a function of both oxidizer flow velocity, V_{ox}, and burning rate. An enhancement of soot from 0.2 to 2.5 ppm occurs with an increase of burning rate from 3, 4 to 5 g/m^{2}s (Cases 1-3) at V_{ox}=0.25 m/s. A decrease of soot from 8 to 2.5 ppm is induced with an increase of V_{ox} from 0.125 to 0.25 m/s for burning rate of 5 g/m^{2}s (Cases 1 and 4). An inverse dependence of soot formation on the mainstream flow rate is predicted. These tendencies are consistent with the experimental observation of Konsur [20] which is based on the global residence time, defined as the ratio of the characteristic flame length, L_f, to the oxidizer velocity. Influence of fuel type as ethylene, propane, propylene, heptane and dodecane on the mean level of soot in the windward direction at V_{ox}=0.25 m/s is shown in Fig.9b. As compared to the ethylene or propane flame (Case 1 or 5) at burning rate of 5 g/m^{2}s, the maximum mean value of soot for propylene (Case 6) increases by a factor of about 3 times due to its strong sooting propensity (cf. Tab.1), and for heptane (Case 7) by a factor of 3.5 times due to its important stratification of smoke layer. The maximum mean value of soot is located far away near the trailing edge at x/L_p=1 except for dodecane. The soot volume fraction of dodecane flame (Case 8) reaches to a maximum at x/L_p=0.5 beyond which its pyrolysis rate tends to zero (cf. Fig.3b), and decays until almost complete absence beyond x/L_p=3.

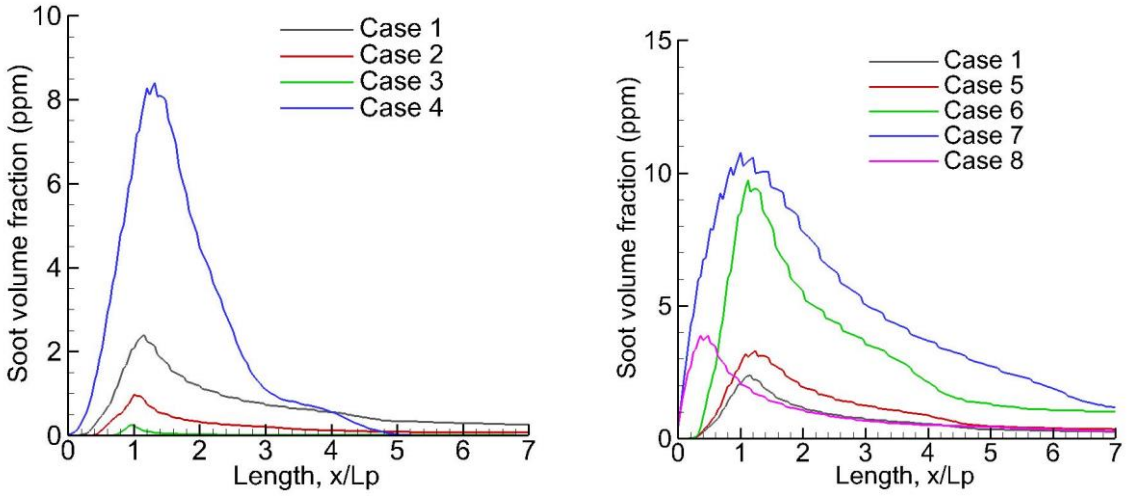

9a) 9b)

Figure 9. Evolution of the mean value of soot volume fraction (ppm) at the steady mode (t=10 s) in the windward direction; a) effect of fuel /oxidizer conditions for ethylene; b) effect of fuel type

When soot is located in a gas-phase cell adjacent to a wall, it can be removed from the gas-phase and deposited onto the surface. The removal of soot deposition onto solid surface at microgravity can impact the visibility for egress and the time for smoke detectors to activate. The soot deposition is computed as a function of soot concentration, Y_s, in a gas-phase cell adjacent to a wall by imposing the following expression:

$$m_s'' = \rho Y_s u_i^{th} \Delta t \qquad (kg/m^2) \qquad (24)$$

For the ethylene flame as presented in Fig.10a, a low soot production (Case 3) in a gas-phase cell adjacent to a wall results in negligible soot deposition, and inversely, a high soot (Case 4) translates to a rise in soot deposition with a value of 0.09 g/m^2. It is worthwhile to note that in the numerical simulation, the porous burner used for ethylene, propane and propylene is not treated as a solid surface, and thus, soot deposition does not takes place. The extent of the soot deposition is between $1<x/L_p<2$ downstream the pyrolysis zone for a fixed burning rate. The fuel type impacts the thermal and soot stratifications, and as a consequence, the soot deposition, as illustrated in Fig.10b. The soot deposition of heptane flame (Case 7) reaches to a maximum of 1 g/m^2 beyond its pyrolysis zone, and decays until almost complete absence beyond $x/L_p=6$ due to a large soot presence of about 30 ppm (cf. Fig.6) in a gas-phase cell adjacent to a wall. The peak value of soot deposition for dodecane (Case 8) occurs in the pyrolysis zone where soot presence is significant (cf. Fig.6). As compared to ethylene (Case 1), the peak of soot deposition increases by a factor of about 11, 4 and 3 times, respectively for heptane (Case 7), dodecane (Case 8) and propylene (Case 6).

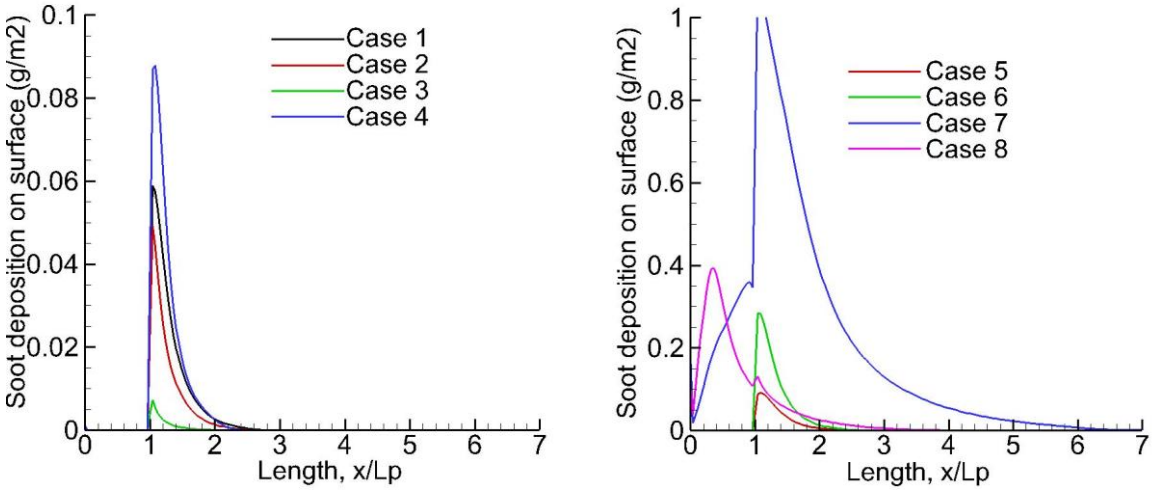

10a) 10b)

Figure 10. Evolution of soot deposition (g/m^2) at the steady mode (t=10 s) over surface in the windward direction; a) effect of fuel/oxidizer conditions for ethylene; b) effect of fuel type

As an illustration, iso-contours of carbon monoxide, CO, on the axis of symmetry for ethylene, heptane and dodecane flames are depicted in Figure 11. The generation of CO is predicted to occur in the fuel-rich reacting region around the fire source, that is, at locations inside the high temperature region. Production of CO is strongly correlated with the trend of the soot generation (cf. Fig.6), and the region of CO in abundance is indicative of an oxygen-starved area. The forward layer carries abundant CO, and the fresh air is capable of providing a quick decay of the CO level downstream starting from $x/L_p=6$. The CO molar fraction reaches to a maximum of about 11% for dodecane (Case 8) and 8% for ethylene (Case 1)/ heptane (Case 7) near the leading edge. This implies that dodecane with a longer carbon chain produces more carbon monoxide than heptane and ethylene. The mean value (cf. Eq.23) of the toxic emissions as CO is examined in the windward direction for ethylene flame as a function of both oxidizer flow velocity, V_{ox}, and burning rate. As shown in Fig.12a for a given fuel as ethylene, the maximum mean value of CO concentration depends mainly on fuel injection rate, and appears practically insensitive to oxidizer flow velocity. An increase in burning rate from 3 to 5 g/m^{2}s correlates to a growth of CO generation from 2.8% (Case 3) to 3.5% (Case 1) due to a decay of combustion efficiency. The extent, x/L_p, of a high CO concentration above 1% increases also from 2.8 to 3.5 with an increase of fuel injection rate from 3 to 5

g/m^{2}s. Response of the mean value of CO, to the change in the fuel type, is presented in Fig.12b. At the oxidizer flow velocity of 0.25 m/s, the strong pyrolysis rate of heptane (cf. Fig.3) significantly reduces the combustion efficiency due to reduction in entrainment of the fresh air into the leading edge, leading to an increase of CO molar fraction to 4%. For dodecane, the maximum mean level of CO undergoes an increase to 5% in the leading edge region, and later, enters quickly the decay phase with a molar fraction of 1% starting from x/L_p=3 due to reduction in its pyrolysis zone (cf. Fig.3b). As compared to ethylene, propane and propylene (Cases 1, 5, 6) with a CO level of about 3%, the peak of CO production increases by a factor of about 30% and 60%, respectively for heptane (Case 7) and dodecane (Case 8).

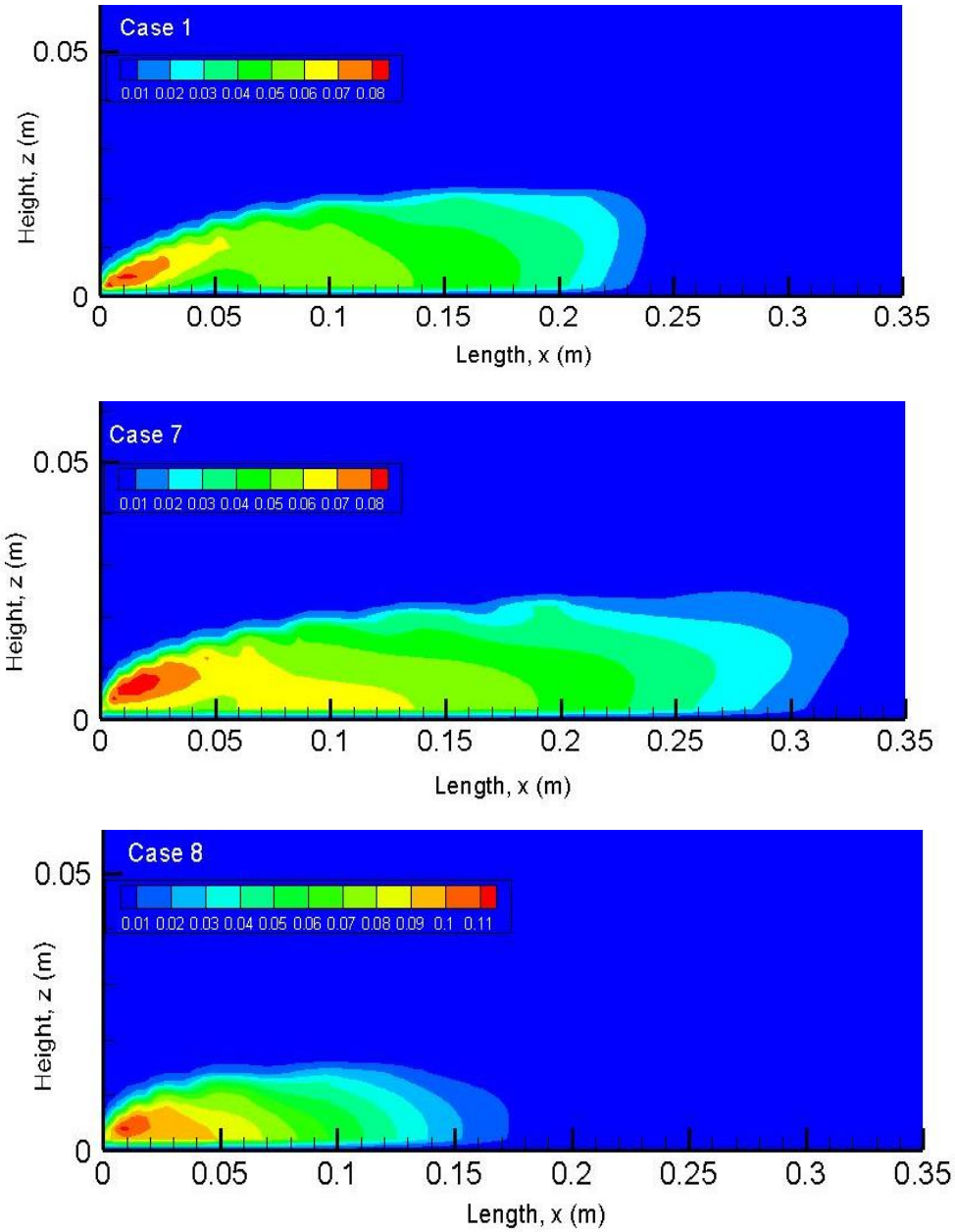

Figure 11. Iso-contours of CO production at the steady mode (t=10 s) for ethylene (Case 1), heptane (Case 7) and dodecane (Case 8)

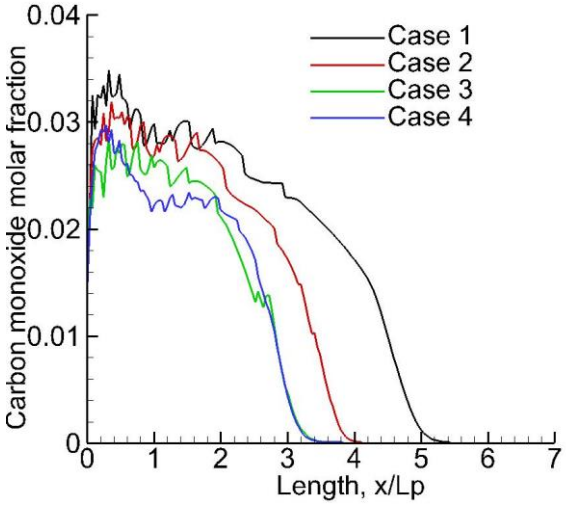

12a)

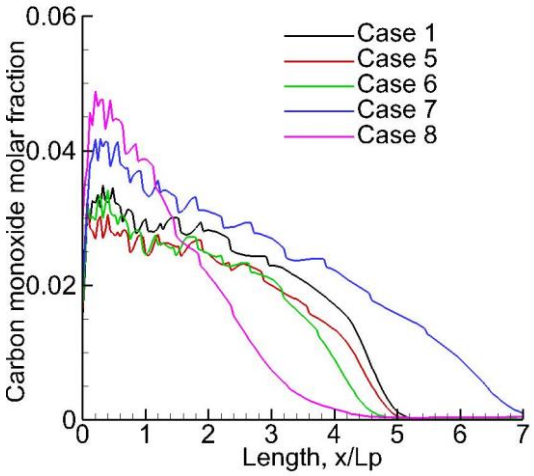

12b)

Figure 12. Evolution of CO production at the steady mode (t=10 s) in the windward direction; a) effect of fuel injection rate and oxidizer flow velocity for ethylene; b) effect of fuel type

Analysis of CO_2 production is also particularly significant considering that CO_2-based fire suppression systems is used on the International Space Station [17]. Fig.13(a, b) shows the mean value of carbon dioxide concentration along forward direction. The calculated spikes of CO_2 originate from the post-processing for assessing its mean value from Eq.23, and can't be considered as physical phenomena. In all the cases, the mean value of CO_2 molar fraction reaches to a maximum of about 10% nearby the region at $x/L_p=4$, implying an identical chemical reactivity in presence of relatively abundant oxygen there. The reduced convective transport at $V_{ox}=0.125$ m/s (Case 4) leads to a rapid decay of CO_2 starting from $x/L_p=3$. Heptane flame (Case 7) facilitates a large presence of CO_2 downstream due to its large visible flame zone (cf. Fig.4). It seems that fuel type and ventilation conditions do not change the trend of CO_2 formation in the forward direction with regarding its mean value.

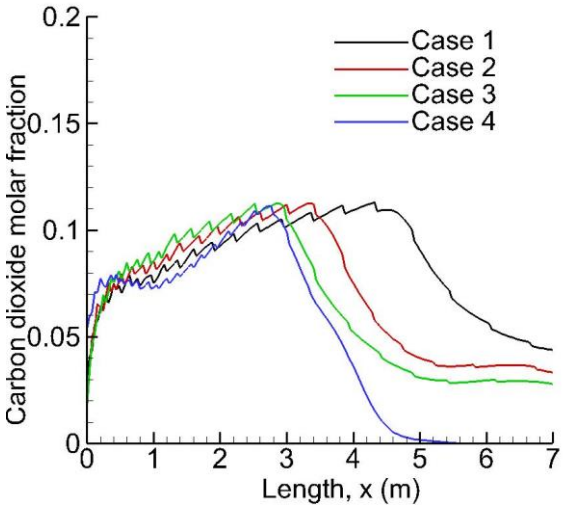

13a)

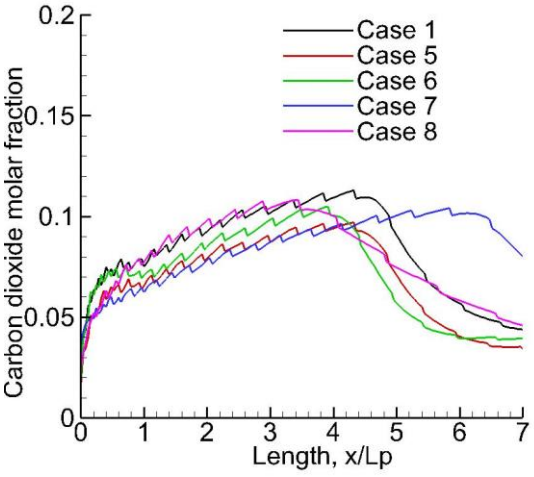

13b)

Figure 13. Evolution of CO_2 production at the steady mode (t=10 s) in the windward direction; a) effect of fuel injection rate and oxidizer flow velocity for ethylene; b) effect of fuel type

Iso-contours of the unburnt hydrocarbons (C_mH_n) due to incomplete reaction on the axis of symmetry for ethylene, heptane and dodecane are depicted in Fig.14. Ethylene with burning rate of 5 g/m^{2}s contributes to the most severe production of unburnt fuels with a peak of 45% nearby the tailing edge due to lack of oxygen. A reduced pyrolysis zone of dodecane allows more incoming air flow towards the tailing edge. This is evidenced by a low level of unburnt hydrocarbon with about 10% due to an improvement of the mixing between oxygen and fuel, which enhances the unburnt C_mH_n oxidation into CO and CO_2. The mean value (cf. Eq.23) of the unburnt hydrocarbons is examined in Fig.15a for ethylene flame as a function of both oxidizer flow velocity, V_{ox}, and burning rate. At V_{ox}=0.25 m/s, an increase of the fuel injection rate from 3 to 5 g/m^{2}s (Cases 1-3) correlates to a rise of the unburnt hydrocarbons from 9% to 14% in molar fraction nearby the tailing edge at x/L_p=1. A reduction in the air supply towards the fire source at V_{ox}=0.125 m/s enhances generation of the unburnt hydrocarbons at the tailing edge with a molar fraction of 21%. Response of the mean value of unburnt hydrocarbons, to the change in the fuel type, is presented in Fig.15b. Dodecane and heptane with a longer carbon chain produces more CO (cf. Fig.12) and less unburnt hydrocarbons (cf. Fig.15) than ethylene, propane and propylene. Usually, whatever the family of hydrocarbons considered, CO formation increases and unburnt hydrocarbons decreases with the length of the carbon chain. In all the cases, a rapid growth of unburnt hydrocarbons at the pyrolysis zone is mainly attributed to the under-ventilated flame there. The unburnt hydrocarbons can be practically suppressed downstream from the fire source for x/L_p beyond 5 thanks to oxidation and dilution. With regarding the ignition risk, the downstream area up to x/L_p=7 remains dangerous for heptane due to its large pyrolysis rate (cf. Fig.3a), because the forward layer carries abundance of unburnt hydrocarbons with a molar fraction of 3%.

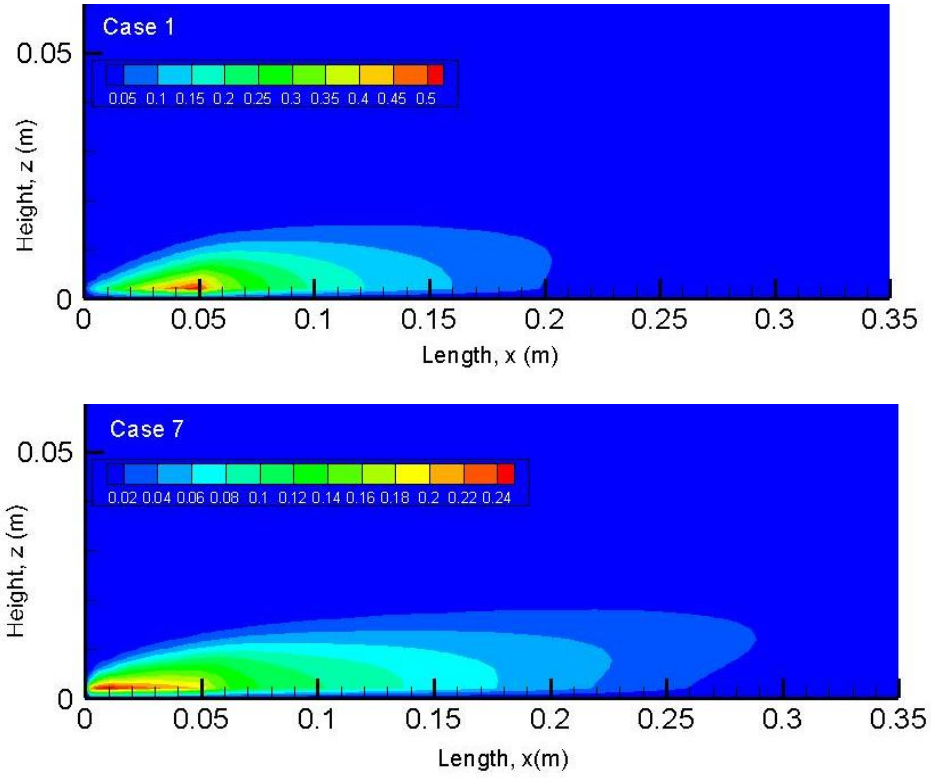

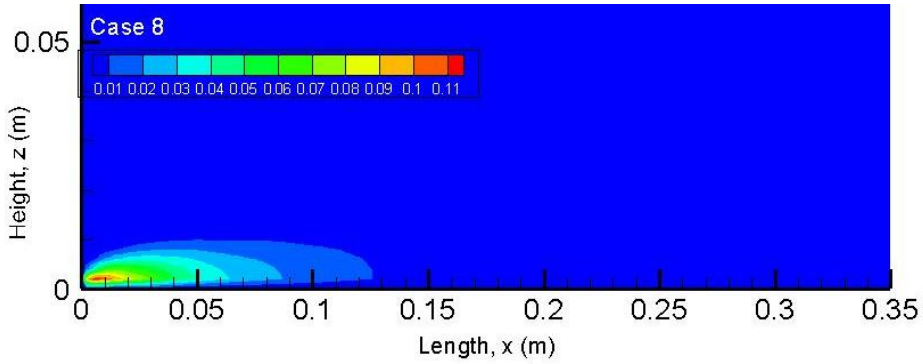

Figure 14. Iso-contours of unburnt hydrocarbons at the steady mode (t=10 s) for ethylene (Case 1), heptane (Case 7) and dodecane (Case 8)

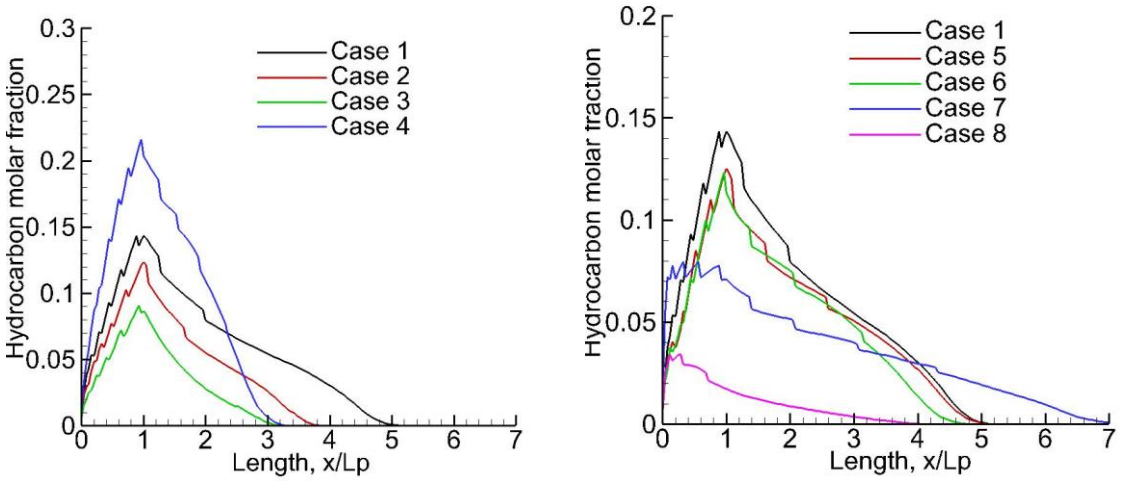

15a) 15b)

Figure 15. Evolution of the mean concentration of unburnt hydrocarbons at the steady mode (t=10 s) in the windward direction; a) effects of fuel injection rate and oxidizer flow velocity for ethylene; b) effects of fuel type

The convection exchanges from the flame to the wall surface is shown in Fig.16(a, b), and a similar trend is found regardless of fuel type. Microgravity flames are typically smooth with a high flame temperature located close to the leading edge (cf. Fig.4), thus promoting a peak of about 40 kW/m^2 in convective heat flux, corresponding to a fraction of the total heat flux higher than 90%. The flame standoff distance increases downstream (cf. Fig.4) and as a result the convective heat flux from the flame to the liquid is reduced due to a sharply decreasing trend of temperature gradient. Given in Fig.17(a, b) is the radiant heat flux over material surface from a flame as a function of fuel/oxidizer conditions for ethylene and fuel type. Radiation heat exchange is a function of both the gas temperature with T^4 dependence and chemical compositions as CO_2, H_2O and soot. The length of the flame (cf. Fig.4) dominates the decrease of the heat flux with distance. The peak of about 10 kW/m^2 in radiant heat flux seems insensitive to the reduction in oxidizer flow velocity (Case 4). Heptane flame clearly enhances the radiation heat flux with a peak value of 12 kW/m^2 over its pyrolysis surface which tends to enhance the thermal degradation of liquid. For heptane, the zone with a high heat flux of about 5 kW/m^2 lasts till x/L_p>5 due to its larger flame area (cf. Fig.4). The radiant heat flux over the exposed surface for propylene increases by a factor of 10% compared to that for propane due to its higher gas temperature (cf. Fig.4) and concentration of emitting species as soot (cf. Fig.9). There is a greater radiant heat feedback from the heptane flame

than that from the other fuel flame, mainly due to its important soot formation (cf. Fig.9) and flame length (cf. Fig.4). Radiation becomes comparatively more important with a fraction of the total heat flux of about 80% once away from the leading edge, because of the absence of natural convection. This implies that, in microgravity, substantial soot radiation in fires can be considered an important mechanism for flame development even for a small flame size. It is worthwhile to note that according to the burning rate (cf. Tab.3 and Fig.3), the heat release rate (HRR) per unit area reaches to a value of about 228 kW/m^2 for ethylene, propane and propylene. A rapid regression rate of heptane (cf. Fig.3a) contributes to an additional energy by a factor of 80% in HRR as compared with that of dodecane (cf. Fig.3b), i.e., about 292 kW/m^2. In all the cases, only about 15% of the heat released from combustion is supplied to the exposed surface, and a major portion is transported by a forward forced convection.

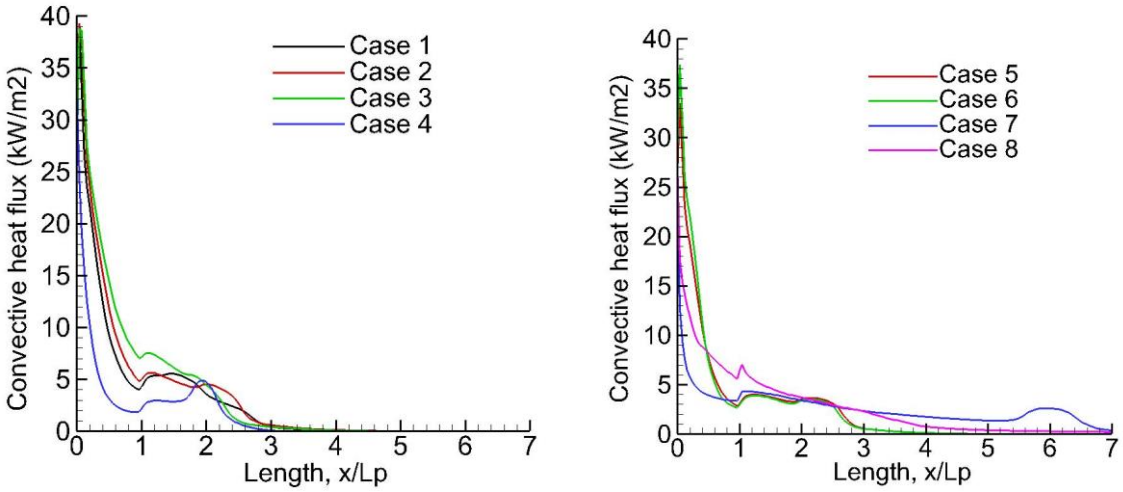

16a) 16b)

Figure 16. Evolution of the convective heat flux at the steady mode (t=10 s) over material surface; a) effects of fuel injection rate and oxidizer flow velocity for ethylene; b) effects of fuel type

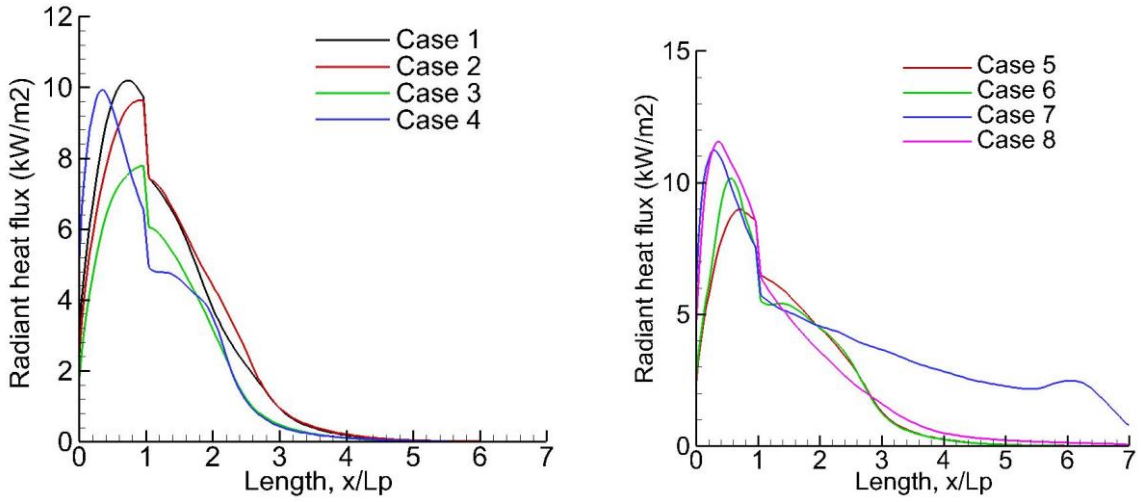

17a) 17b)

Figure 17. Evolution of the radiant heat flux at the steady mode (t=10 s) over material surface; a) effects of fuel injection rate and oxidizer flow velocity for ethylene; b) effects of fuel type

4. Conclusions

The purpose of the overall research consists in identifying the importance of fuel type on toxic emissions such as soot, CO and unburnt hydrocarbons for a diffusion flame established in a shear boundary layer under weightless conditions. The behavior of soot production is reasonably well predicted by using LSP inception model as compared with the measured soot volume fraction during parabolic flights. This provides a general and practical solution for soot modeling in multi-fueled fires.

These findings indicate that in microgravity, substantial soot radiation in fires can be considered an important mechanism for flame development even for a small flame size with a fraction of the total heat flux of about 80%. A concurrent spreading flame over dodecane in microgravity approaches a non-growing, steady state and a limiting pyrolysis length due to its high boiling temperature. Heptane flame produces a more dangerous environment compared to dodecane, with an increase in the flame length by a factor of 2.3 times because of its low boiling temperature. The length of the flame dominates the decrease of the heat flux with distance, and as a result, the pyrolysis rate of liquid fuel. There are marked differences in the spatial distribution of the pyrolysis rate between a purely-buoyant flow on Earth and a purely-forced flow in microgravity. At very-low-flow speeds in microgravity, the pyrolysis rate depends on the radiation flux once away from the leading edge, an important distinction compared to the case at Earth gravity with a high flow speed which normally depends on only convection flux. Compared with Earth gravity flames, microgravity flames have much greater tendencies to emit large toxic emissions, which could result in untenable thermal conditions and environmental pollution in spacecraft, even for a smaller flame size because of the absence of natural convection. Dodecane with a longer carbon chain produces more carbon monoxide which reaches to a maximum of about 11% in molar fraction as compared to other fuels. The maximum mean value of CO concentration depends mainly on pyrolysis rate, and appears practically insensitive to oxidizer flow velocity. Dodecane and heptane with a longer carbon chain produces more CO and less unburnt hydrocarbons than ethylene, propane and propylene. A rapid regression rate of heptane contributes to an additional energy by a factor of 80% in heat release rate as compared to dodecane. In all the cases, only about 15% of the heat generated by an exothermic chemical reaction is supplied to the exposed surface, and a large portion of energy is convected by the forward gas flow. The spatial distributions of toxic emissions and heat transfer are crucial to the performance based designs of fire protection and safety on board of spacecraft.

With regarding the ignition risk, a large downstream area remains dangerous in microgravity, because of the abundance of soot, CO and unburnt hydrocarbons. Accelerating fire may happen occasionally due to a sudden supply in oxygen at hidden area where combustible gas can be accumulated in sufficient concentration. On the basis of global extinction/ignition criteria, the current numerical tool is useful through the post-processing for assessing auto-ignition of unburnt pyrolyzates. The future investigation aims also to properly take into account the effects of heated liquid-phase flow due to the surface tension gradients for the prediction of a flame spread over thick liquid layer. An experimental database on heat flux in microgravity, owing to pyrolysis of an inflammable liquid, is needed for further validation of the numerical tool.

Funding and/or Conflicts of interests/Competing interests

I confirm that this theoretical research in the manuscript doesn't provide conflicts of interests/competing interests with any people and organism.

Data Availability Statements

The datasets generated during and/or analysed during the current study are available from the corresponding author on reasonable request.

References

[1] Torero, J.L., Bonneau, L., Most, J.M. and Joulain, P., The effect of gravity on a laminar diffusion flame established over a horizontal plate, 25th Symposium (international) on Combustion (Pittsburgh: The Combustion Institute), pp.1701-1709 (1994).

[2] Rouvreau, S., Torero, J.L and Joulain, P., Numerical evaluation of boundary layer assumptions for laminar diffusion flames in micro gravity, Combustion Theory and Modelling, Vol.9, n° 2:137-158 (2005).

[3] Fuentes, A., Legros, G., Claverie, A., Joulain, P., Vantelon and J.P., Torero, J.L., Influence of the oxidizer velocities on the sooting behaviour of non-buoyant laminar diffusion flame, 31th Symposium (international) on Combustion (Pittsburgh: The Combustion Institute), 2685-2692 (2007).

[4] Legros, G., Joulain, P., Vantelon, J.P., Fuentes, A. and Torero, J.L., Soot volume fraction measurements in a three dimensional laminar diffusion flame established in microgravity, Combustion Science and Technology, 178-180 (2006).

[5] H. Y. WANG, J.L.F. Merino and P. Dagaut, Effects of soot formation on shape of a nonpremixed laminar flame established in a shear boundary layer in microgravity, Journal of Physics: Conference Series, Vol.327, 012038 (2011).

[6] S. Rouvreau, P. Joulain, H.Y. Wang, P. Cordeiro and J. Torero, Numerical evaluation of boundary layer assumptions used for the prediction of the stand-off distance of a laminar diffusion flame, 29th Symposium International on Combustion, The Combustion Institute, Pittsburgh, 1685-1692 (2002).

[7] David L. Urban, Paul Ferkul, Sandra Olson, Gary A. Ruff, John Easton, James S. T'ien, Ya-Ting T. Liao, Chengyao Li, Carlos Fernandez-Pello, Jose L. Torero, Guillaume Legros, Christian Eigenbrod, Nickolay Smirnov, Osamu Fujita, Sébastien Rouvreau, Balazs Toth, Grunde Jomaas. Flame spread: Effects of microgravity and scale. Combustion and Flame 199 (2019) 168-182.

[8] Urban, D. L., Yuan, Z. G., Sunderland. P. B., Voss, J. E., Lin, K. C., Dai, Z., Sun, K., and Faeth G. M., Structure and soot properties of non-buoyant ethylene/air laminar jet diffusion flames, AIAA 36:1346-1360 (1998).

[9] Creenberg, P S. and Ku, J. C., Soot volume fraction maps for normal and reduced gravity laminar acetylene jet diffusion flame, Combust. Flame 108:227-230 (1997).

[10] A. Guibaud, J.M. Citerne, J.M. Orlac'h, O. Fujita, J.-L. Consalvi, J.L. Torero, G. Legros, Broadband modulated absorption/emission technique to probe sooting flames: Implementation, validation, and limitations, Proc. Combust. Inst. 37 (2019) 3959-3966.
[11] Guibaud A., Citerne J.M., Consalvi J.L., Torero J.L., Fujita O., Kikuchi M., Ferkul P.V., Smirnov N.N., Jomaas G., Toth B., Rouvreau S., Legros G., Accessing the soot-related radiative heat feedback in a flame spreading in microgravity: optical designs and associated limitations, Proceedings of the Combustion Institute, vol. 38, N°3, pp. 4805-4814 (2021).
[12] A. Guibaud, J. L. Consalvi, J.M. Orlac'h, O. J.M. Citerne and G. Legros, Soot production and radiative heat transfer in opposed flame spread over a polyethylene insulated wire in microgravity, Fire Technol. (2019).
[13] L. Hu, Y. Zhang, K. Yoshioka, H. Izumo, O. Fujita, Flame spread over electric wire with high thermal conductivity metal core at different inclination, Proc. Combust. Inst. 35 (3):2607-2614 (2015).
[14] Jomaas G., Torero J.L., Eigenbrod C., Niehaus J., Olson S.L., Ferkul P.V., Legros G., Fernandez-Pello A.C., Cowlard A.J., Rouvreau S., Smirnov N., Fujita O., T'Ien J.S., Ruff G.A., Urban D.L. Fire safety in space-beyond flammability testing of small samples. Acta Astronautica, vol. 109 (2015), pp. 208-216.
[15] J.M. Citerne, H Dutilleul, K Kizawa, M Nagachi, O Fujita, M. Kikuchi, G. Jomaas, S. Rouvreau, J.L. Torero, G. Legros, Fire safety in space - Investigating flame spread interaction over wires, Acta Astronaut. 126 (2016) 500-509.

[16] Olson, S.L., Mechanisms of microgravity flame spread over a thin solid fuel: oxygen and opposed flow effects, Combust. Sci. Technol 76:233-249 (1991).

[17] Paul D. Ronney, Understanding combustion processes through microgravity research, 27th Symposium (international) on Combustion (Pittsburgh: The Combustion Institute), 2485-2493 (1998).
[18] Ramachandra, P. A., Altenkirch, R. A., Bhattacharjee, S., Tang, L., Sacksteder, K., Wolverton, M. K., The behavior of flame spreading over thin solids in microgravity, Combust. Flame 100:71-84 (1995).
[19] Bhattacharjee, S., Mtenkirch, R. A., and Sacksteder, K.,J. The effect of ambient pressure on flame spread over thin cellulosic fuel in a quiescent microgravity environment, Heat Transfer 118:181-190 (1996).
[20] Konsur, B., Megaridis and C.M., Griffin, D.W., Soot aerosol properties in laminar soot-emitting microgravity nonpremixed flames, Combustion and Flame 118 (4), 509-520 (1999).

[21] G. Legros, A. Fuentes, S. Rouvreau, P. Joulain, B. Porterie, J.L. Torero, Transport mechanisms controlling soot production inside a non-buoyant laminar diffusion flame, Proc. Combust. Inst. 32: 2461–2470 (2009).
[22] V.V. Tyurenkova and M.N. Smirnova, Material combustion in oxidant flows: self-similar solutions, Acta Astronautica 120 (2016) 129-137.

[23] Smirnov N.N., Tyurenkova V.V., Smirnova M.N. Laminar diffusion flame propagation over thermally destructing material Acta Astronautica, Pergamon Press Ltd. (United Kingdom), vol. 109 (2015), pp. 217-224.

[24] Leung, K.M., Lindstedt, R.P. and Jones, W.P., A simplified reaction mechanism for soot formation in nonpremixed flames, Combustion and Flame, 289-305 (1991).

[25] T. Beji, J. Zhang, M. A. Delichatsios, Determination of soot formation rate from laminar smoke point measurements, Combustion Science and Technology 180 (5) 927940 (2008).

[26] K. Mcgrattan, R. Mcdermott, S. Hostikka and J. Floyd, Fire Dynamics Simulator (Version 6), User's guide, NIST Special Publication (2018).

[27] C.L. Beyler, Major species production by diffusion flames in a two-layer compartment fire environment, Fire Safety Journal, 10 (1986), 47-56.

[28] C. K. Westbrook and F.L. Dryer, Simplified reaction mechanisms for the oxidation of hydrocarbon fuels in flames, Combustion Science and Technology, 27:31-43 (1981).

[29] J. Andersen, C.L. Rasmussen, T. Giselsson and P. Glarborg, Global combustion mechanisms for use in CFD modeling under oxy-fuel conditions, Energy and Fuels, 23(3):1379-1389 (2009).

[30] Moss, J.B., Stewart, C.D., Young, K.J., Modelling soot formation and burnout in a high temperature laminar diffusion flame burning under oxygen-enriched conditions, Combustion and Flame, 101:491-500 (1995).

[31] Lee, K.B., Thring, M.W. and Beer, J.M., On the rate of combustion of soot in a laminar soot flame, Combustion and Flame, 6: 137-145 (1962).

[32] A. Murty Kanury, Introduction to Combustion Phenomena, New York: Gordon, ISBN 0-677-02690-0 (1984).

[33] Coutin M, Most JM, Delichatsios MA, Delichatsios MM., Flame heights in wall fires : effects of width, confinement and pyrolysis length. Proceedings of the Sixth International Symposium on Fire Safety Science, Poitiers, France, 729-739 (1999).

[34] Fujita, O., Ito, K., Ito, H. and Takeshita, Y., Effect of thermophoretic force on soot agglomeration process in diffusion flame under microgravity, 4th NASA International Microgravity Combustion Workshop, 217-222 (1997).